



Structural, Optical, and Magnetic Properties of Mn-Doped Nickel Ferrite ($\text{Ni}_{1-x}\text{Mn}_x\text{Fe}_2\text{O}_4$) Thin Films Deposited by Jet Nebulizer Spray Pyrolysis Technique

K. Sasikumar¹ · R. Bharathikannan² · G. Sujithkumar² · S. Raja³ · G. Johnsy Arputhavalli⁴ · M. Vidhya⁵ · R. Marnadu² · R. Suresh²

Received: 20 May 2021 / Accepted: 20 June 2021 / Published online: 2 July 2021
© The Author(s), under exclusive licence to Springer Science+Business Media, LLC, part of Springer Nature 2021

Abstract

In this work, pure and Mn-doped nickel ferrite ($\text{Ni}_{1-x}\text{Mn}_x\text{Fe}_2\text{O}_4$, $x=0, 3, 6, 9,$ and 12 wt%) thin films were prepared using facile nebulizer spray pyrolysis technique. The effect of Mn concentration on the structural, optical, and magnetic properties was studied. The XRD pattern confirms the cubic spinel structure of $\text{Ni}_{1-x}\text{Mn}_x\text{Fe}_2\text{O}_4$ thin films and reveals the preferred orientation along the (311) direction for each film. Moreover, the average crystallite size (D) is found to increase from 13 to 30 nm with increasing Mn concentration. The FESEM micrographs exhibit randomly arranged plate-like and rice-like grains. The elements such as Mn, Ni, Fe, and O are confirmed by the EDX analysis. The optical band gap energy (E_g) varies between 2.90 and 3.60 eV. The $\text{Ni}_{1-x}\text{Mn}_x\text{Fe}_2\text{O}_4$ film prepared with 3 wt% of Mn exhibits superior ferrimagnetic behavior with the highest value of η_B (57.31) due to the high crystallinity, packing density, and smooth surface of the film. The present work shows that the facile nebulizer spray pyrolysis technique can produce high-quality $\text{Ni}_{1-x}\text{Mn}_x\text{Fe}_2\text{O}_4$ thin films with good magnetic properties.

Keywords Spinel ferrites · Spray pyrolysis · Magnetic properties · Rice-like · XRD

1 Introduction

Ferrite—the oxide magnetic material, has been widely studied by various researchers because of its exceptional magnetic characteristics. The material is known for its adaptability to suit definite applications by modifying its basic characteristics, including coercivity, electrical conductivity,

and saturation magnetization [1]. In recent years, ferrite is considered a prospective candidate for applications in magnetic fluids, magnetic recording, non-volatile memory devices, catalysts, magnetically-targeted delivery of drugs, hyperthermia, magnetic resonance imaging enhancement, microwave absorbers, sensors, and pigments [2–7]. The nickel ferrite (NiFe_2O_4), belonging to inverse spinel cubic structure, is one of the extensively applied materials for storage devices owing to its significant coercivity and good saturation magnetization property at room temperature [8, 9]. In addition, electrical resistivity and high dielectric constant have made it a suitable material for transformer core and high-frequency device applications [11]. Also, the soft magnetic nature of nickel ferrite has been exploited in hyperthermia applications [10].

The nickel ferrite crystal consists of two interpenetrating sublattices A and B which are tetrahedrally and octahedrally coordinated, respectively. The A site is completely engrossed with Fe^{3+} ions, whereas the B site is equally shared by Fe^{3+} and Ni^{2+} ions. The antiparallel orientation of spins of varying magnitude at the A site and B site induces the ferrimagnetic nature in the nickel ferrite crystal [12]. The nickel

✉ K. Sasikumar
sasiphy2012@gmail.com

¹ Department of Physics, Sri Ramakrishna Engineering College, Coimbatore, Tamil Nadu 641022, India

² Department of Physics, Sri Ramakrishna Mission Vidyalyaya College of Arts and Science, Coimbatore, Tamil Nadu 641020, India

³ Department of Physics, Bharathidasan University, Tiruchirappalli, Tamil Nadu 620024, India

⁴ Department of Physics, Coimbatore Institute of Technology, Coimbatore, Tamil Nadu 641014, India

⁵ Department of Physics, Government Arts College for Women, Dindigul, Tamil Nadu 624 208, India

ferrite, in the form of thin film, exhibits various physical properties suitable for novel applications in diverse fields. The state of design, characterization, and augmented properties of thin films are highly influenced by the synthesis methods. To synthesize ferrite thin films, researchers so far have used various deposition methods, namely, magnetron sputtering (single and multitarget), pulsed laser deposition, spin coating, and electroplating (or ferrite plating) [13–20]. Among the different techniques, the spray pyrolysis method is extensively used for fabricating mixed thin films due to its simplicity in process, huge area of deposition, uniformity in thickness, and low energy for the film preparation [21]. The parameters such as annealing temperature, substrate temperature, pH, and grain size, followed during synthesis of nickel ferrite thin films, will significantly influence the film properties which can be further modified by doping of divalent/trivalent ions. The magnetic properties of the nickel ferrite are greatly affected by doping of various metals such as Co, Mn, Ag, Ce, Li, and Nd [22–27]. The NiFe_2O_4 has a cubic structure. In the case of Mn-doped nickel ferrite ($\text{Ni}_{1-x}\text{Mn}_x\text{Fe}_2\text{O}_4$), the Ni^{2+} metal ions are replaced by Mn^{2+} ions according to the value of x . It is also expected that Mn^{2+} ions occupy the octahedral sites (B site) and the Ni^{2+} ions are constantly diffused between octahedral (B site) and tetrahedral (A site) sites. In the present work, $\text{Ni}_{1-x}\text{Mn}_x\text{Fe}_2\text{O}_4$ ($x=0, 3, 6, 9, \text{ and } 12 \text{ wt}\%$) thin films have been deposited on preheated glass substrates using nebulizer spray pyrolysis technique and subsequently annealed at 600°C . The film samples are characterized for their microstructural, optical, and magnetic properties at room temperature.

2 Experimental Details

2.1 Preparation of Mn-Doped Nickel Ferrite Thin Films

All the chemicals were purchased from Merck and used without further purification. For the preparation of $\text{Ni}_{1-x}\text{Mn}_x\text{Fe}_2\text{O}_4$ thin films, manganese (II) chloride tetrahydrate ($\text{MnCl}_2 \cdot 4\text{H}_2\text{O}$, 99.99%), ferric chloride anhydrous (FeCl_3 , 99.99%), and nickel chloride (NiCl_2 , 98%) were used as starting materials. Initially, 1.18845 g of nickel chloride and 1.6221 g of ferric chloride anhydrous was dissolved in 100 ml of deionized water to make the pure solution. After that, the solution was stirred for 2 h in ambient conditions using a magnetic stirrer. To prepare manganese-doped nickel ferrite ($\text{Ni}_{1-x}\text{Mn}_x\text{Fe}_2\text{O}_4$), the concentration of manganese (II) chloride tetrahydrate was chosen as 3, 6, 9, and 12 wt% in the solution. The borosilicate glass slides (1.35 mm thickness) were used as substrates.

Prior to deposition process, the substrates were cleaned using detergent, isopropanol, and deionized water in

ultrasonicator. The cleaned substrates were dried in air and used for spray deposition. During the process, the substrate temperature was maintained at 300°C in the air atmosphere. The compressed air was used as a carrier gas. The distance between spray nozzle and substrate was fixed as 5 cm. To obtain Mn-doped nickel ferrite ($\text{Ni}_{1-x}\text{Mn}_x\text{Fe}_2\text{O}_4$) thin films, the prepared solution was sprayed on hot substrate for 3 min using a jet nebulizer with spray rate of 0.5 ml/min. The as-prepared films were annealed at 600°C for 1 h to improve the crystallinity. The obtained film samples were well-adherent and compact to substrate.

2.2 Characterization

The structural properties of $\text{Ni}_{1-x}\text{Mn}_x\text{Fe}_2\text{O}_4$ ($x=0, 3, 6, 9, \text{ and } 12 \text{ wt}\%$) thin films were examined by the X-ray diffractometer (X-Pert Pro, PANalytical) with $\text{Cu K}\alpha_1$ radiation ($\lambda = 1.54056 \text{ \AA}$). Surface morphology of the samples was investigated by the field emission scanning electron microscope (Sigma with Gemini column, CARL ZEISS). The chemical compositions were identified using energy dispersive X-ray spectroscopy (Nano Xflash detector, BRUKER). The optical properties of thin film samples were studied using the UV–Vis spectrophotometer (JASCO UV–Vis–NIR spectrophotometer, V-770PC). The magnetic properties were analyzed using the vibrational sample magnetometer (Lakeshore VSM 7410S) at room temperature.

3 Results and Discussion

3.1 Structural Properties

Figure 1 illustrates the XRD patterns of $\text{Ni}_{1-x}\text{Mn}_x\text{Fe}_2\text{O}_4$ ($x=0, 3, 6, 9, \text{ and } 12 \text{ wt}\%$) thin films. The diffraction peaks at 2θ ($^\circ$) = 30.2, 35.6, 43.3, 53.8, 57.3, and 63 are attributed to (220), (311), (400), (422), (511), and (440) crystallographic planes, which confirm the formation of cubic spinel structure [11]. The most intense peak observed along the (311) plane direction is also an indication of the spinel structure. These results are in accordance with the earlier reports and the standard reference pattern of NiFe_2O_4 (JCPDS card no. 74–2081) [11]. The peaks become narrow with an increase in the Mn concentration. The strong and sharp diffraction peaks indicate the high crystallinity of the prepared thin films. Moreover, no impurity phases are identified in the XRD patterns of $\text{Ni}_{1-x}\text{Mn}_x\text{Fe}_2\text{O}_4$ thin films. The diffraction peaks along (220), (400), and (440) crystallographic planes are due to the cation sharing [28].

From the XRD patterns of $\text{Ni}_{1-x}\text{Mn}_x\text{Fe}_2\text{O}_4$ thin films, it is noticed that the small peak shift occurs particularly along the (220) and (311) planes in the ferrite lattice. And apparent shift is observed for all the peaks towards the lower

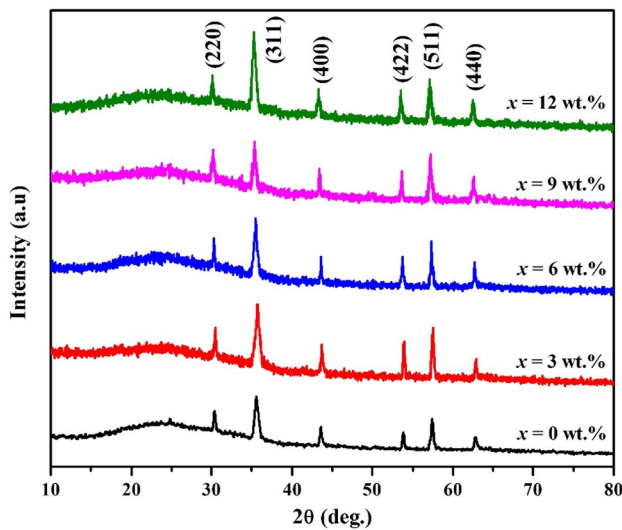


Fig. 1 XRD patterns of $\text{Ni}_{1-x}\text{Mn}_x\text{Fe}_2\text{O}_4$ ($x=0, 3, 6, 9,$ and 12 wt%) thin films

diffraction angle. This peak shift with the increase of doping concentration is due to the large ionic radius of Mn^{2+} (0.83 \AA) when compared to Fe^{3+} (0.67 \AA) and Ni^{2+} (0.72 \AA) ions [28, 29]. The shift occurs at lower angle position can be attributed to the distribution of cations throughout the nickel-manganese (Ni-Mn) ferrites [11]. The crystallite size (D) of $\text{Ni}_{1-x}\text{Mn}_x\text{Fe}_2\text{O}_4$ thin films were calculated from Debye-Scherrer formula,

$$D = \frac{0.89\lambda}{\beta \cos\theta} \quad (1)$$

where D is the crystallite size, λ is the wavelength ($\lambda=0.15418 \text{ nm}$), β is the full-width at half-maximum (FWHM) of the diffraction peak, and θ is the angle of diffraction. The calculated average crystallite sizes of $\text{Ni}_{1-x}\text{Mn}_x\text{Fe}_2\text{O}_4$ films are found to be gradually increasing from 13 to 30 nm with increasing Mn concentration up to 6 wt%. The 6 wt% Mn-doped nickel ferrite ($\text{Ni}_{1-x}\text{Mn}_x\text{Fe}_2\text{O}_4$) thin film exhibits a high crystallinity when compared to the pure NiFe_2O_4 and other Mn-doped nickel ferrite thin films.

The variation of crystallite size may be due to the replacement of smaller Ni^{2+} ions by larger Mn^{2+} ions and cation distribution [29]. Besides, an increase in the population of Mn^{2+} and a decrease in the Fe^{3+} cations cause a lattice expansion. This is supported by Vinosha et al. in the case of Dy-doped nickel ferrite nanocrystals [28].

The various chemical compositions of $\text{Ni}_{1-x}\text{Mn}_x\text{Fe}_2\text{O}_4$ for $x=0, 3, 6, 9,$ and 12 wt% are given in Table 1. The microstructural parameters like microstrain (ϵ), dislocation density (δ), and stacking fault (SF) were calculated by using the following relations [11, 28, 29], and the values are tabulated.

$$\delta = \frac{1}{D^2} \quad (2)$$

$$\epsilon = \frac{\lambda}{D \sin\theta} - \frac{\beta}{\tan\theta} \quad (3)$$

$$\text{SF} = \left[\frac{2\pi^2}{45(3 \tan\theta)^{1/2}} \right] \beta \quad (4)$$

From Table 1, it is observed that the dislocation density initially decreases in the lattice system and then increases in the case of 9 wt% Mn ion concentration. Among the various concentrations, the 6 wt% Mn-doped nickel ferrite thin film has the minimum dislocation density of 0.287×10^{16} lines/ m^2 when compared to other films. The mean values of microstrain (ϵ) and stacking fault (SF) are gradually reduced for Mn-doped nickel ferrite ($\text{Ni}_{1-x}\text{Mn}_x\text{Fe}_2\text{O}_4$) films up to 6 wt% concentration. Subsequently, the values are slightly increased for 9 and 12 wt% Mn-doped nickel ferrite ($\text{Ni}_{1-x}\text{Mn}_x\text{Fe}_2\text{O}_4$) films. The average stacking fault (SF) of the films is found to be varying from 0.571×10^{-2} to 1.257×10^{-2} . Thus, XRD results clearly indicate that the variation in Mn concentration can strongly boost the crystallinity and the structural parameters of $\text{Ni}_{1-x}\text{Mn}_x\text{Fe}_2\text{O}_4$ films.

3.2 Surface Morphology and Composition Analysis

The two-dimensional (2D) morphology of spray-deposited $\text{Ni}_{1-x}\text{Mn}_x\text{Fe}_2\text{O}_4$ thin films was studied by FESEM analysis,

Table 1 Structural parameters of $\text{Ni}_{1-x}\text{Mn}_x\text{Fe}_2\text{O}_4$ ($x=0, 3, 6, 9,$ and 12 wt%) thin films

Mn concentration (wt%)	Chemical composition	Average crystallite size D (nm)	Average dislocation density δ ($\times 10^{16}$ lines/ m^2)	Average microstrain ϵ ($\times 10^{-3}$)	Average stacking fault SF ($\times 10^{-2}$)
0	NiFe_2O_4	13.07	1.041	3.237	1.257
3	$\text{Ni}_{0.97}\text{Mn}_{0.03}\text{Fe}_2\text{O}_4$	16.67	0.521	2.341	0.792
6	$\text{Ni}_{0.94}\text{Mn}_{0.06}\text{Fe}_2\text{O}_4$	29.68	0.287	1.662	0.571
9	$\text{Ni}_{0.91}\text{Mn}_{0.09}\text{Fe}_2\text{O}_4$	14.2	0.498	1.645	1.071
12	$\text{Ni}_{0.88}\text{Mn}_{0.12}\text{Fe}_2\text{O}_4$	13.2	0.831	2.583	0.987

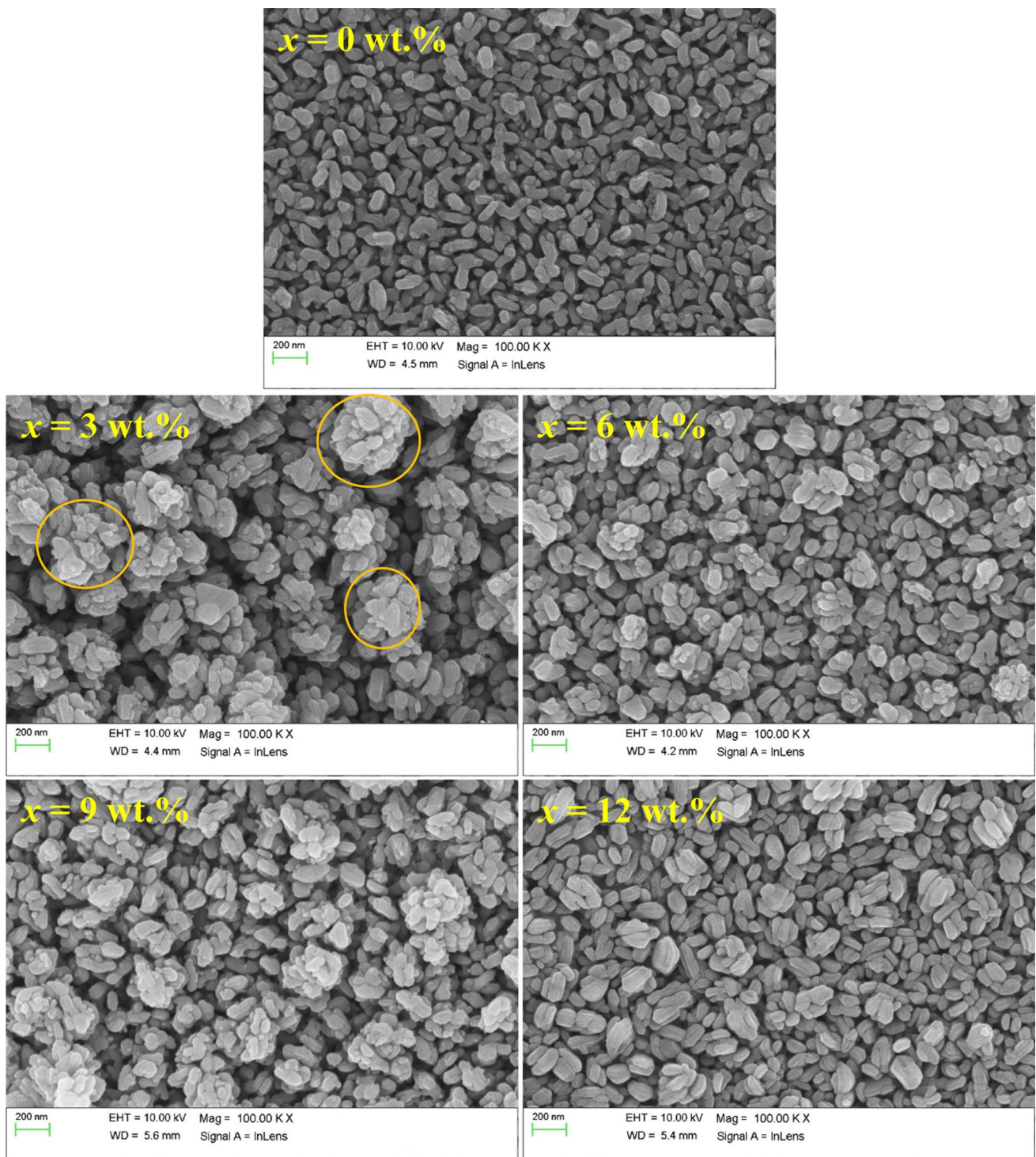


Fig. 2 FESEM micrographs of $\text{Ni}_{1-x}\text{Mn}_x\text{Fe}_2\text{O}_4$ ($x=0, 3, 6, 9,$ and 12 wt%) thin films

and the micrographs are shown in Fig. 2. For the pure nickel ferrite film, the randomly arranged plate-like and rice-like grains are observed with thickness ranging from 20 to 150 nm. Interestingly, the grains are found to be bounded tightly after incorporating Mn cations in the NiFe_2O_4

lattice. This result is attributed to the agglomeration of NiFe_2O_4 crystallites caused by the Mn ions. Particularly, $\text{Ni}_{1-x}\text{Mn}_x\text{Fe}_2\text{O}_4$ film deposited with 3 wt% Mn exhibits a largely-agglomerated grain-like surface. The length of the grains is reduced for 3, 6, and 9 wt% Mn-doped nickel ferrite

($\text{Ni}_{1-x}\text{Mn}_x\text{Fe}_2\text{O}_4$) thin films. The grain size was analyzed for all the $\text{Ni}_{1-x}\text{Mn}_x\text{Fe}_2\text{O}_4$ films using image j software, and the histograms of grain size distribution are shown in Fig. 3. The grain size of 102, 145, 165, 132, and 148 nm is obtained for 0, 3, 6, 9, and 12 wt% of Mn doping, respectively. Figure 4 indicates the EDX spectra of the pure and Mn-doped nickel ferrite ($\text{Ni}_{1-x}\text{Mn}_x\text{Fe}_2\text{O}_4$) films for different doping concentrations of Mn. From the EDX spectra, the expected elements such as Mn, Ni, Fe, and O are confirmed. Both wt% and at.% of Mn are found to increase with the increase of Mn concentration. Similarly, the Fe^{3+} concentration

increases up to 6 wt% of Mn and then decreases. The peaks of other elements such as C, Al, P, and Ca are attributed to the constituents of glass substrate.

3.3 Optical Properties

The UV–Visible absorption spectra of $\text{Ni}_{1-x}\text{Mn}_x\text{Fe}_2\text{O}_4$ ($x=0, 3, 6, 9,$ and 12 wt%) thin films are shown in Fig. 5. All the films exhibit a strong absorption peak between the wavelengths of 260 and 285 nm, after which the absorption gently reduces up to 400 nm. The band at 260 nm (i.e.,

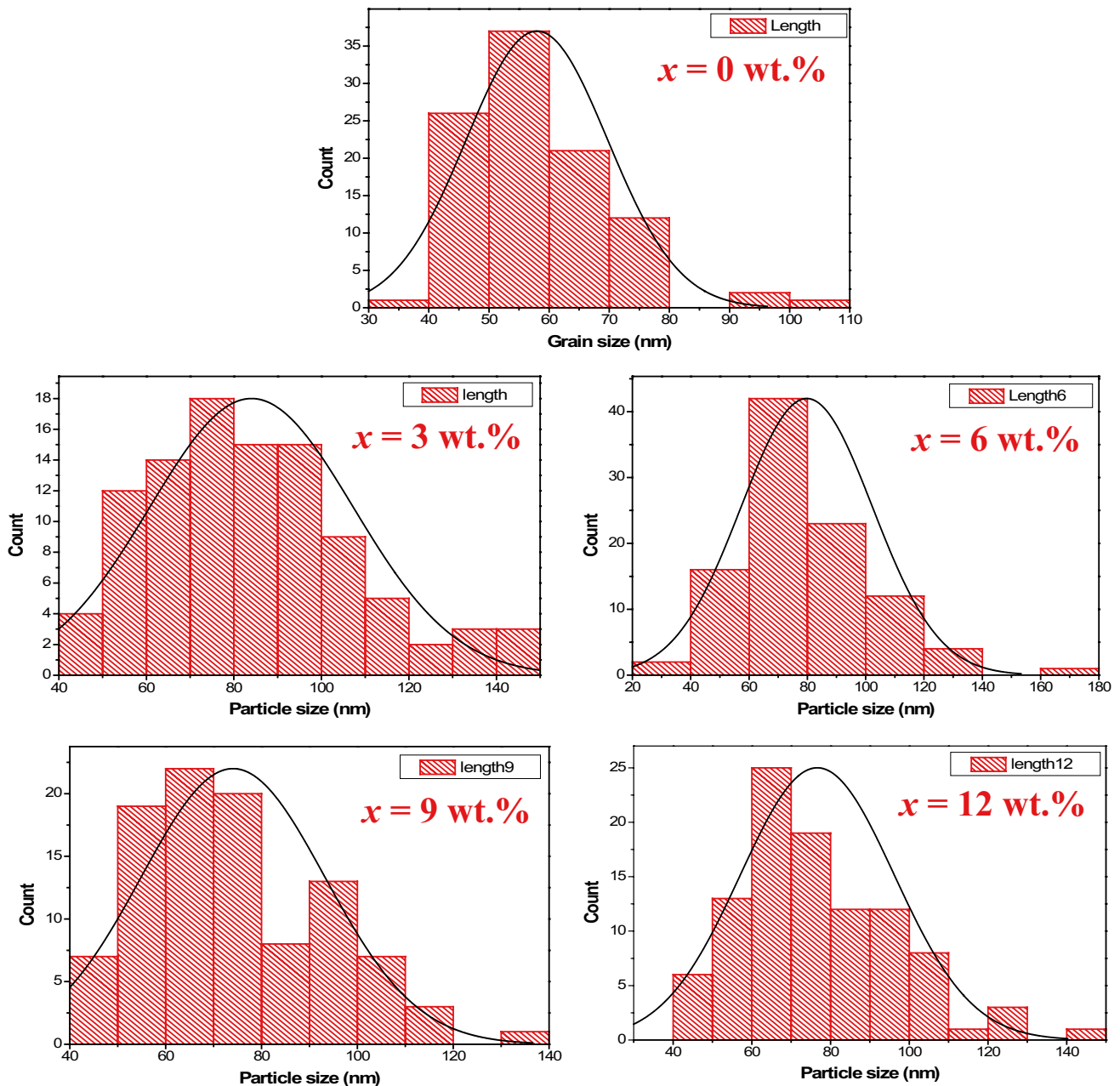


Fig. 3 Histograms of the grain size distribution for $\text{Ni}_{1-x}\text{Mn}_x\text{Fe}_2\text{O}_4$ ($x=0, 3, 6, 9,$ and 12 wt%) thin films

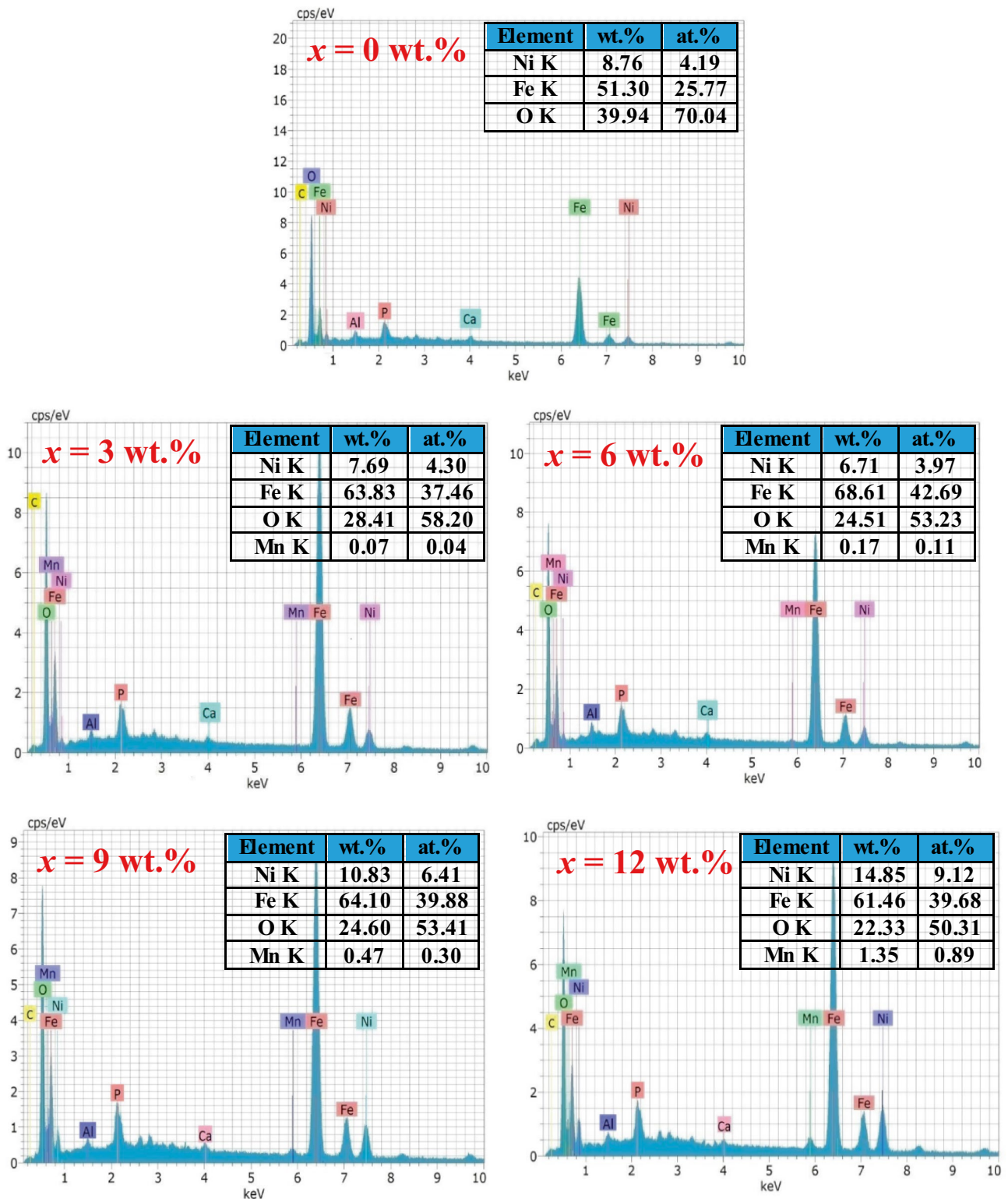


Fig. 4 EDX spectra of $\text{Ni}_{1-x}\text{Mn}_x\text{Fe}_2\text{O}_4$ ($x=0, 3, 6, 9,$ and 12 wt%) thin films

UV region) is attributed to charge transfer transitions from Fe^{3+} to O^{2-} in NiFe_2O_4 thin films [30]. The absorption peak intensity increases in the UV region for all the

$\text{Ni}_{1-x}\text{Mn}_x\text{Fe}_2\text{O}_4$ films compared to the pure NiFe_2O_4 thin film. This is attributed to the substitution of Mn ions into nickel ferrite lattice which increases the oxygen vacancy in

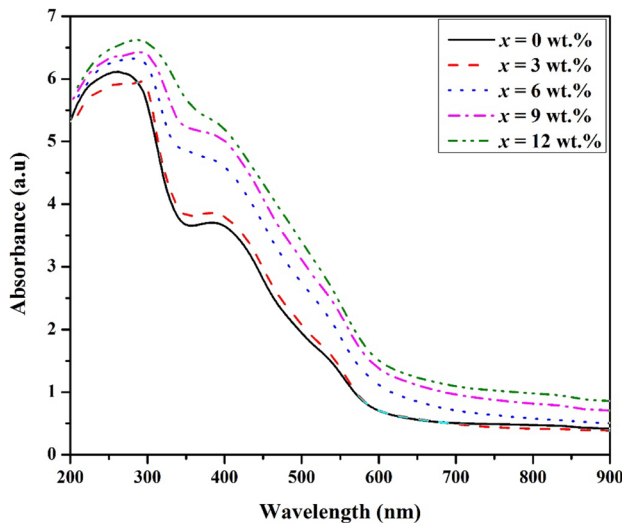


Fig. 5 Absorption spectra of $\text{Ni}_{1-x}\text{Mn}_x\text{Fe}_2\text{O}_4$ ($x=0, 3, 6, 9,$ and 12 wt%) thin films

the Mn-doped nickel ferrite ($\text{Ni}_{1-x}\text{Mn}_x\text{Fe}_2\text{O}_4$) thin films [30]. Interestingly, Harish et al. have reported similar changes in Nd-doped nickel ferrite ($\text{NiFe}_{2-x}\text{Nd}_x\text{O}_4$) nanofilms prepared by chemical co-precipitation method [31].

From Fig. 5, it is seen that the absorption spectra of all the $\text{Ni}_{1-x}\text{Mn}_x\text{Fe}_2\text{O}_4$ films slightly shifts towards a longer wavelength region (i.e., red shift) with respect to the pure NiFe_2O_4 film. The red shift may be attributed to the extra subband energy formed by doping Mn^{2+} ions in the nickel ferrite films; i.e., a partial replacement of Ni^{2+} ions by Mn^{2+} ions causes some electronic states to be formed into the band gap of NiFe_2O_4 . The optical band gap (E_g) of the prepared thin films was determined by the Tauc’s relation, and the values are given in Table 2.

$$(\alpha h\nu)^n = A(h\nu - E_g) \tag{5}$$

where α is the absorption coefficient, h is the Planck’s constant, ν is the Photon energy, A is the constant relative to the material, and E_g is the band gap. The band gap energy can be derived by extrapolating the linear portion of the $(\alpha h\nu)^2$ vs. $h\nu$ plot to $(\alpha h\nu)^2=0$ as shown in Fig. 6. The calculated band gap energy (E_g) is found to be varying in the range of

Table 2 Band gap energy (E_g) of $\text{Ni}_{1-x}\text{Mn}_x\text{Fe}_2\text{O}_4$ ($x=0, 3, 6, 9,$ and 12 wt%) thin films

Mn concentration (wt.%)	Band gap energy E_g (eV)
0	3.60
3	3.56
6	3.35
9	3.15
12	2.90

2.90–3.60 eV, and the values are in good agreement with the earlier reports [30–33]. The band gap energy gradually decreases with respect to an increase in the Mn concentration, which is attributed to the quantum confinement effect. Besides, the decrease in band gap energy may be ascribed to an improvement in the crystallinity of the films and reduced crystal defects [32]. It is seen that the average crystallite size increases when Ni^{2+} ions are substituted with Mn^{2+} ions. Further, due to the large ionic radius of Mn^{2+} compared to Ni^{2+} , the ionic interactions get stronger as the Mn^{2+} concentration increases [33]. Hence, the density of energy level between the valance band and conduction band decreases as well as the lattice constant increases.

3.4 Magnetic Properties

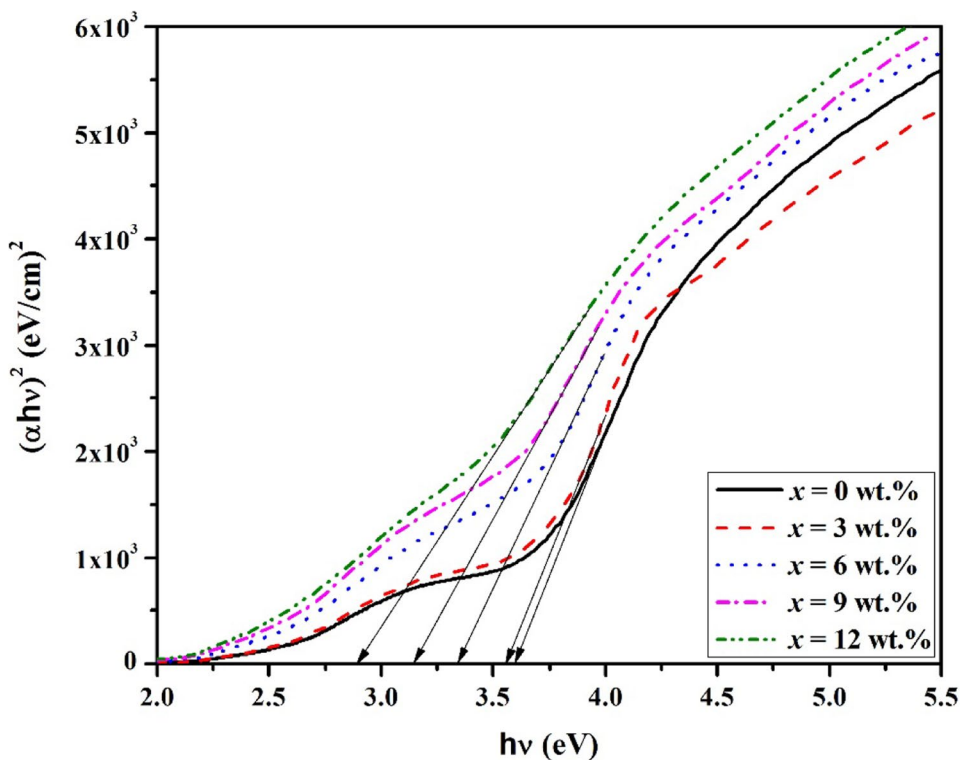
The magnetic properties of Mn-doped nickel ferrite ($\text{Ni}_{1-x}\text{Mn}_x\text{Fe}_2\text{O}_4$) thin films have been analyzed at room temperature using a vibrating sample magnetometer in the applied field ranging from -15 to $+15$ kOe. The magnetic properties of the spinel ferrite thin films strongly depend on the factors like substrate temperature, annealing temperature, microstructure, and chemical composition [34]. The influence of cationic stoichiometry and their occupancy in the specific sites can modify the magnetic properties of $\text{Ni}_{1-x}\text{Mn}_x\text{Fe}_2\text{O}_4$ thin films. The hysteresis curves of Mn-doped nickel ferrite thin films prepared with various Mn concentrations are depicted in Fig. 7. It is observed that the prepared thin films have a soft ferrimagnetic nature due to its narrow hysteresis cycle. When compared to other doping concentrations, the 3 wt% Mn-doped $\text{Ni}_{1-x}\text{Mn}_x\text{Fe}_2\text{O}_4$ film exhibits superior ferrimagnetic behavior due to its higher crystallinity, packing density, and smooth surface. Several factors like synthesis technique, chemical composition, cation distribution, crystallite size, microstructure, and canting angle control the shape and width of the hysteresis curve [35]. The magnetic parameters like remanent magnetization (M_r), saturation magnetization (M_s), coercivity (H_c), remanence ratio (R), Bohr magneton number (η_B), and magneto-crystalline anisotropy (K) of the prepared thin films were calculated, and the values are listed in Table 3. The experimental Bohr magneton number was determined using the following relation [36].

$$\eta_B = \frac{M_w \times M_s}{\mu_B \times N_A} \tag{6}$$

where M_w is the molecular weight of the each composition, M_s is the saturation magnetization, μ_B is the Bohr magneton, and N_A is the Avogadro’s number.

The anisotropy constant is related to the coercivity through Brown’s relation [36].

Fig. 6 Plot of $(\alpha h\nu)^2$ vs. $h\nu$ for $\text{Ni}_{1-x}\text{Mn}_x\text{Fe}_2\text{O}_4$ ($x=0, 3, 6, 9,$ and 12 wt%) thin films



$$H_c = \frac{2K}{\mu_B M_s} \tag{7}$$

The values of M_s , M_r , η_B , and K increase, whereas the values of H_c and R decrease for the $\text{Ni}_{1-x}\text{Mn}_x\text{Fe}_2\text{O}_4$ thin

film prepared with 3 wt% Mn concentration. The same phenomena are distorted for higher doping concentrations of Mn. The super-exchange interaction between the lattice sites of Mn and nickel ferrites deteriorates the values of coercivity and saturation magnetization. This

Fig. 7 Hysteresis curves of $\text{Ni}_{1-x}\text{Mn}_x\text{Fe}_2\text{O}_4$ ($x=0, 3, 6, 9,$ and 12 wt%) thin films

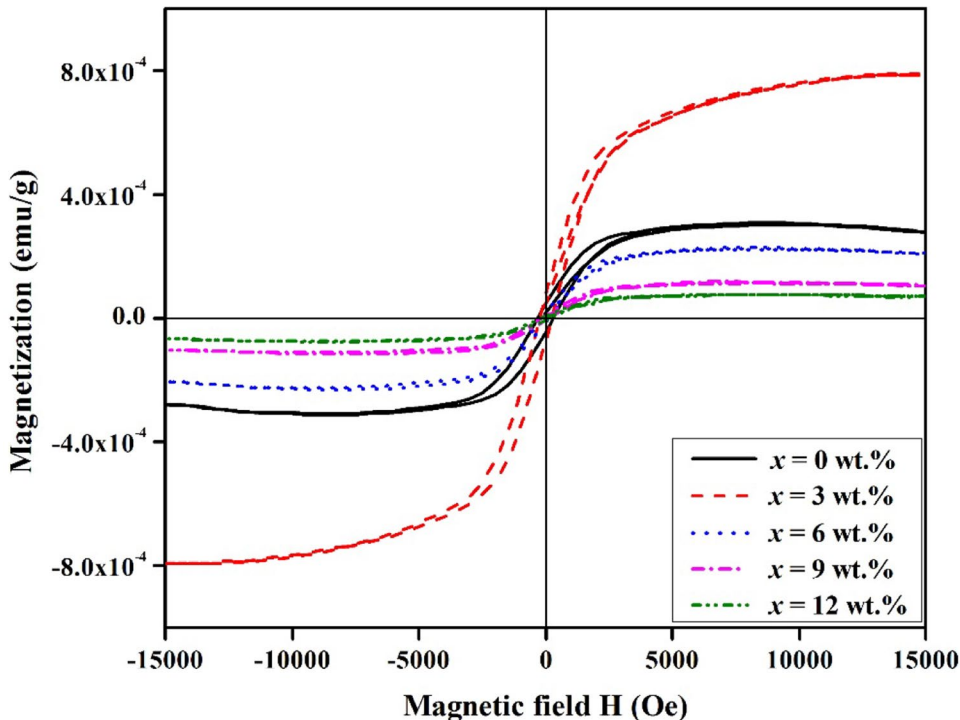


Table 3 Magnetic parameters of Ni_{1-x}Mn_xFe₂O₄ (x=0, 3, 6, 9, and 12 wt%) thin films

Mn concentration (wt%)	Saturation magnetization M _s × 10 ⁻⁶ (emu/g)	Remanent magnetization M _r × 10 ⁻⁶ (emu/g)	Coercivity H _c (Oe)	Remanence ratio (R)	Bohr magneton number η _B (μ _B)	Anisotropy constant K (erg/cc)
0	304.18	38.51	286.2551	0.1266	21.78	25,203.49
3	688.70	66.32	216.3871	0.0840	57.31	39,399.64
6	226.59	8.98	88.3303	0.0396	16.71	5793.25
9	114.75	4.35	69.2184	0.0379	8.58	2299.04
12	74.68	3.28	56.7901	0.0440	5.66	1227.58

super-exchange interaction decreases the saturation magnetization due to the displacement of low magnetic Mn²⁺ ions into high magnetic Ni²⁺ ions [37]. The experimental Bohr magneton number strongly depends on saturation magnetization and coercivity. The highest value of η_B is 57.31 for the Ni_{1-x}Mn_xFe₂O₄ film prepared with 3 wt% Mn concentration, which is due to the high magnetic nature. The reduction in coercivity also reduces the energy of magneto-crystalline anisotropy. Magneto-crystalline structure and texturing, the stress induced during the film growth, and grain size are the significant factors for the reduction of anisotropy energy. Nevertheless, the difference in angular momentum between Mn²⁺ and Ni²⁺ ions is the main reason for the decrease in anisotropy. The contribution of Mn²⁺ ions in the magneto-crystalline anisotropy is annihilated due to its zero angular momentum, it replaces some of the Ni²⁺ ions which weakens the spin–orbit coupling, hence the anisotropy and coercivity decreases [38]. From the above discussions, the continuous displacement of Ni²⁺ ions and Mn²⁺ ions at the cubic lattice site reduces the anisotropy energy of Mn-doped nickel ferrite thin films. From these results, it is concluded that the Ni_{1-x}Mn_xFe₂O₄ thin film prepared with 3 wt% Mn shows better saturation magnetization and magneto-crystalline anisotropy, which can lead to data storage applications.

4 Conclusion

In summary, Ni_{1-x}Mn_xFe₂O₄ (x=0, 3, 6, 9, and 12 wt%) thin films were deposited by jet nebulizer spray pyrolysis technique. The structural, optical, and magnetic properties of the prepared films were investigated by XRD, FESEM, EDX, UV, and VSM. The cubic spinel structure of Ni_{1-x}Mn_xFe₂O₄ films was confirmed by XRD profile. The maximum average crystallite size of 30 nm was obtained for 6 wt% Mn doping. The FESEM micrographs confirmed the presence of randomly-arranged plate-like and rice-like grains. From EDX spectral analysis, the elements such as Mn, Ni, Fe, and O were confirmed. A maximum absorbance with minimum band gap energy of 2.90 eV was observed for the 12 wt% Mn concentration. From the VSM results, the calculated value of

Bohr magneton number (η_B) is 57.31 for the Ni_{1-x}Mn_xFe₂O₄ thin film prepared with 3 wt% Mn concentration due to its high magnetic nature. Hence, it is suggested that the Ni_{1-x}Mn_xFe₂O₄ thin film prepared at 3 wt% is highly appropriate for data storage applications in RAM and ROM.

References

- Rao, P., Godbole, R.V., Phase, D.M., Chikate, R.C., Bhagwat, S.: Ferrite thin films: Synthesis, characterization and gas sensing properties towards LPG. *Mater. Chem. Phys.* **149–150**, 333–338 (2015)
- Hu, W., Qin, N., Wu, G., Lin, Y., Li, S., Bao, D.: Opportunity of spinel ferrite materials in nonvolatile memory device applications based on their resistive switching performances. *J. Am. Chem. Soc.* **134**, 14658–14661 (2012)
- Giri, J., Pradhan, P., Sriharsha, T., Bahadur, D.: Preparation and investigation of potentiality of different soft ferrites for hyperthermia applications. *J. Appl. Phys.* **97**, 10Q916 (2005)
- Yeh, T.C., Zhang, W., Ildstad, S.T., Ho, C.: In vivo dynamic MRI tracking of rat T-cells labeled with superparamagnetic iron-oxide particles. *Magn. Reson. Med.* **33**, 200–208 (1995)
- Li, B.W., Shen, Y., Yue, Z.X., Nan, C.W.: Enhanced microwave absorption in nickel/hexagonal-ferrite/polymer composites. *Appl. Phys. Lett.* **89**, 132504 (2006)
- Belloy, E., Thurre, S., Walckiers, E., Sayah, A., Gijs, M.A.M.: Introduction of powder blasting for sensor and microsystem applications. *Sens. Actuators. A* **84**, 330–337 (2000)
- Reddy, C.V.G., Manorama, S.V., Rao, V.J.: Semiconducting gas sensor for chlorine based on inverse spinel nickel ferrite. *Sens. Actuators. B* **55**, 90–95 (1999)
- Lüders, U., Barthélémy, A., Bibes, M., Bouzouane, K., Fusil, S., Jacquet, E., Contour, J.-P., Bobo, J.-F., Fontcuberta, J., Fert, A.: NiFe₂O₄: A versatile spinel material brings new opportunities for spintronics. *Adv. Mater.* **18**, 1733–1736 (2006)
- Kumari, K., Kumar, R., Barman, P.B.: Tuning of structural, magnetic and optical properties of NiFe₂O₄ films by implementing high magnetic fields. *Thin Solid Films.* **712**, 138321 (2020)
- Jacob, B.P., Kumar, A., Pant, R.P., Singh, S., Mohammed, E.M.: Influence of preparation method on structural and magnetic properties of nickel ferrite nanoparticles. *Bull. Mater. Sci.* **34**, 1345–1350 (2011)
- Ghayour, H., Abdellahi, M., Ozada, N., Jabbrzare, S., Khandan, A.: Hyperthermia application of zinc doped nickel ferrite nanoparticles. *J. Phys. Chem. Solids.* **111**, 464–472 (2017)
- Hao, A., Ismail, M., He, S., Qin, N., Chen, R., Rana, A.M., Bao, D.: Enhanced resistive switching and magnetic properties of Gd-doped NiFe₂O₄ thin films prepared by chemical solution deposition method. *Mater. Sci. Eng. B* **229**, 86–95 (2018)

13. Jin, C., Zheng, D.X., Li, P., Mi, W.B., Bai, H.L.: Resistive switching in reactive cosputtered MFe_2O_4 ($M = Co, Ni$) films. *Appl. Surf. Sci.* **263**, 678–681 (2012)
14. Liang, Y.-C., Hsia, H.-Y.: Growth and crystallographic feature-dependent characterization of spinel zinc ferrite thin films by RF sputtering. *Nanoscale Res. Lett.* **8**, 537 (2013)
15. Liu, W., Tan, G., Ren, H., Xia, A.: Multiferroic $BiFe_{1-x}TM_xO_3/NiFe_2O_4$ ($TM = Mn, Cr$) thin films: structural, electrical and magnetic properties. *J. Alloys Compd.* **647**, 351–356 (2015)
16. Rai, R.C., Wilser, S., Guminiak, M., Cai, B., Nakarmi, M.L.: Optical and electronic properties of $NiFe_2O_4$ and $CoFe_2O_4$ thin films. *Appl. Phys. A: Mater. Sci. Process.* **106**, 207–211 (2012)
17. Himcinschi, C., Vrejoiu, I., Salvan, G., Fronk, M., Talkenberger, A., Zahn, D.R.T., Rafaja, D., Kortus, J.: Optical and magnetooptical study of nickel and cobalt ferrite epitaxial thin films and submicron structures. *J. Appl. Phys.* **113**, 084101 (2013)
18. Matzen, S., Moussy, J.-B., Wei, P., Gatel, C., Cezar, J.C., Arrio, M.A., Sainctavit, Ph., Moodera, J.S.: structure, magnetic ordering, and spin filtering efficiency of $NiFe_2O_4$ (111) ultrathin films. *Appl. Phys. Lett.* **104**, 182404 (2014)
19. Bandgar, S.B., Vadiyar, M.M., Ling, Y.-C., Chang, J.-Y., Han, S.-H., Ghule, A.V., Kolekar, S.S.: Metal precursor dependent synthesis of $NiFe_2O_4$ thin films for high-performance flexible symmetric supercapacitor. *ACS Appl. Energy Mater.* **1**, 638–648 (2018)
20. Seifkar, S., Tabei, A., Sacht, E., Rawdanowicz, T., Bassiri-Gharb, N., Schwartz, J.: Growth of (111) oriented $NiFe_2O_4$ polycrystalline thin films on Pt (111) via sol-gel processing. *J. Appl. Phys.* **112**, 063908 (2012)
21. Chavan, A.R., Birajdar, S.D., Chilwar, R.R., Jadhav, K.M.: Structural, morphological, optical, magnetic and electrical properties of Al^{3+} substituted nickel ferrite thin films. *J. Alloys Compd.* **735**, 2287–2297 (2018)
22. Yao, H., Ning, X., Zhao, H., Hao, A., Ismail, M.: Effect of Gd-doping on structural, optical, and magnetic properties of $NiFe_2O_4$ As-prepared Thin Films via Facile Sol-Gel Approach. *ACS Omega* **6**, 6305–6311 (2021)
23. Hao, A., Ismail, M., He, S., Qin, N., Huang, W., Wu, J., Bao, D.: Ag-NPs doping enhanced resistive switching performance and induced changes in magnetic properties of $NiFe_2O_4$ thin films. *RSC Adv.* **7**, 46665–46677 (2017)
24. Hao, A., He, S., Qin, N., Chen, R., Bao, D.: Ce-doping induced enhancement of resistive switching performance of $Pt/NiFe_2O_4/Pt$ memory devices. *Ceram. Int.* **43**, S481–S487 (2017)
25. Ding, K., Zhao, J., Zhou, J., Zhao, Y., Chen, Y., Liu, L., Wang, L., He, X., Guo, Z.: A novel material $Li_2NiFe_2O_4$: Preparation and performance as anode of lithium ion battery. *Mater. Chem. Phys.* **177**, 31–39 (2016)
26. Bharathi, K.K., Vemuri, R.S., Ramana, C.V.: Dysprosium-substitution induced changes in the structure and optical properties of nickel ferrite ($NiFe_2O_4$) thin films. *Chem. Phys. Lett.* **504**, 202–205 (2011)
27. Shinde, T.J., Gadkari, A.B., Vasambekar, P.N.: Influence of Nd^{3+} substitution on structural, electrical and magnetic properties of nanocrystalline nickel ferrites. *J. Alloys Compd.* **513**, 80–85 (2012)
28. Vinosha, P.A., Deepapriya, S., Rodney, J.D., Krishnan, S., Das, S.J.: Investigation on elastic, magnetic, optical and electrical impedance properties of Dysprosium doped nickel ferrite nanocrystals. *J. Nanosci. Nanotechnol.* **19**, 8020–8035 (2019)
29. Kesavamoorthi, R., Raja, C.R.: Studies on the properties of manganese substituted nickel ferrite nanoparticles. *J. Supercond. Novel Magn.* **29**, 2729–2734 (2016)
30. Singh, S., Hitkari, G., Pandey, G.: Synthesis and characterization of cadmium doped nickel ferrite ($Ni_{0.6}Cd_{0.4}Fe_2O_4$) nanoparticles and its optical properties. *Int. J. Sci. Eng. Res.* **8**, 1630–1635 (2017)
31. Harish, K.N., Naik, H.S.B., Kumar, P.N.P., Viswanath, R.: Optical and photocatalytic properties of solar light active Nd-substituted Ni ferrite catalysts: for environmental protection. *ACS Sustainable Chem. Eng.* **9**, 1143–1153 (2013)
32. Tahir, M.B., Iqbal, T., Hassan, A., Ghazal, S.: Wet chemical Coprecipitation synthesis of nickel ferrite nanoparticles and their characterization. *J. Inorg. Organomet. Polym. Mater.* **27**, 1430–1438 (2017)
33. Sharifi, S., Yazdani, A., Rahimi, K.: Incremental substitution of Ni with Mn in $NiFe_2O_4$ to largely enhance its supercapacitance properties. *Sci. Rep.* **10**, 10916 (2020)
34. Verma, K.C., Singh, V.P., Ram, M., Shah, J., Kotnala, R.K.: Structural, microstructural and magnetic properties of $NiFe_2O_4$, $CoFe_2O_4$ and $MnFe_2O_4$ nanoferrite thin films. *J. Magn. Mater.* **323**, 3271–3275 (2011)
35. Ashima, Sanghi, S., Agarwal, A., Reetu: Rietveld refinement, electrical properties and magnetic characteristics of Ca–Sr substituted barium hexaferrites. *J. Alloys Compd.* **513**, 436–444 (2012)
36. Chavan, A.R., Shisode, M.V., Undre, P.G., Jadhav, K.M.: Influence of Cr^{3+} substitution on structural, morphological, optical, and magnetic properties of nickel ferrite thin films. *Appl. Phys. A: Mater. Sci. Process. A* **125**, 472 (2019)
37. Chauhan, C.C., Kagdi, A.R., Jotania, R.B., Upadhyay, A., Sandhu, C.S., Shirsath, S.E., Meena, S.S.: Structural, magnetic and dielectric properties of Co-Zr substituted M-type calcium hexagonal ferrite nanoparticles in the presence of α - Fe_2O_3 phase. *Ceram. Int.* **44**, 17812–17823 (2018)
38. Humbe, A.V., Nawle, A.C., Shinde, A.B., Jadhav, K.M.: Impact of Jahn Teller ion on magnetic and semiconducting behaviour of Ni-Zn spinel ferrite synthesized by nitrate-citrate route. *J. Alloys Compd.* **691**, 343–354 (2017)

Publisher's Note Springer Nature remains neutral with regard to jurisdictional claims in published maps and institutional affiliations.